Scientia Iranica D (2022) 29(1), 193–207

Sharif University of Technology
Scientia Iranica
Transactions D: Computer Science & Engineering and Electrical Engineering
http://scientiairanica.sharif.edu

Control and stability analysis of VSC-HVDC-based transmission system connected to offshore wind farms

A. Haghi and M. Rahimi*

Department of Electrical and Computer Engineering, University of Kashan, Kashan, P.O. Box 87317-53153, Iran.

Received 19 February 2019; received in revised form 10 August 2019; accepted 14 September 2019

KEYWORDS
Integration of wind power generation; Voltage Source Converters (VSC); High-Voltage Direct-Current (HVDC) lines; Offshore wind farms; DC-link voltage regulation.

Abstract. Offshore Wind Farms (WFs) with significant capacities have been installed recently all over the world. In order to transmit the WF power to the onshore grid, High Voltage Direct Current (HVDC) transmission system is appropriate technology. This paper analytically studies the impact of system parameters, controllers, and operating conditions on the dynamic behavior of HVDC transmission systems based on three-level neutral point clamped Voltage Source Converters (VSC). Also, it investigates modeling, control, and stability analysis of VSC-HVDC systems connected to the offshore wind farms. The VSC-HVDC system comprises offshore and onshore converters and high-voltage dc transmission lines. The paper extracts VSC-HVDC system dynamics on the dc side and argues the interaction between onshore converter control and HVDC transmission line dynamics. Moreover, the paper presents a controller design for the dc-link voltage regulation by the onshore converter and examines the impacts of HVDC line length and dc voltage control bandwidth (BW) on the system stability through the modal analysis and time domain simulations.

1. Introduction

Offshore wind farms have many advantages over traditional onshore wind farms. For instance, the availability of higher wind speed, simplicity of high wind power transmission, and limited available inland locations to install new wind farms in some countries make offshore wind farms a promising alternative [1]. Hence, offshore wind farms have had a significant growth in recent years. 3.148 GW of offshore wind power capacity was connected to the grid over the year 2017 in Europe. This corresponds to 560 new offshore wind turbines across 17 wind farms [2]. Also, 1.558 GW of a new offshore wind power capacity was connected to the grid during the year 2016 in Europe, which is a 48.4% decrease compared to 2015 [3].

In order to facilitate the transfer of large electrical power generated by offshore wind farms to the grid, High Voltage Direct Current (HVDC) system plays an important role. Multilevel Voltage Source Converter (MVSC) topologies have received raised attention in recent years in order to make a connection between offshore wind power and the local grid [4]. HVDC system with fast and flexible power flow control provides electrical grid reliability and security. In addition, offshore wind farms are usually located far from the local grid. Therefore, the power produced by offshore wind farms needs long transmission lines to transmit the generated electricity to the consumers. For such an offshore grid, the application of High-

*. *Corresponding author. Tel.: +9831 55913469*
E-mail addresses: a.haghi1989@yahoo.com (A. Haghi); mrahimi@kashanu.ac.ir (M. Rahimi)

doi: 10.24200/sci.2019.52980.2984

Voltage Alternating Current (HVAC) technology is not possible, because with the increase in transmission distance, the reactive power flow is higher due to line capacitances, which will result in significant line losses [5-7]. Therefore, HVDC transmission line is considered a key technology for this purpose. The main feature of the transmission system based on VSC-HVDC is its ability for independent control of active and reactive power flow in each of the AC grids, as addressed in [8–12].

Over the last few years, HVDC transmission systems were based on Current Source Converters (CSCs). CSC uses a line-commutated switching device, which is subject to some limitations. For example, it needs reactive power compensation devices resulting in a bulk converter station. Modern HVDC transmission systems employ VSCs that use self-commutated devices. It is implied that in VSC, the current can lead or lag the ac voltage; thus, the converter consumes or supplies reactive power to the connected ac grid eliminating the reactive power compensation devices [13,14]. Furthermore, higher switching frequency of Pulse-Width Modulation (PWM) reduces the filtering requirements and power flow can be reversed without the need to reverse the dc-link voltage. All these advantages show that the VSC is an appropriate option for HVDC transmission systems.

Several papers have dealt with the modeling, control, and performance analysis of the VSC-HVDC systems connected to offshore wind farms. The author [15] investigated the operation and control of an offshore wind farm connected to an HVDC system and adopted a fuzzy logic controller for the offshore VSC station. In this paper, stability of the HVDC system under developed control schemes is dynamically and transiently investigated. In [16], modal and stability analysis of a VSC-HVDC based offshore wind farm was presented to study the nature of different oscillatory modes that were present in the wind farm system. However, researchers [15-16] did not examine the impact of HVDC system parameters on system stability. The study [17] dealt with the coordinated control of a VSC-HVDC system for inertia support of the main grid. The inertia support was performed through the utilization of wind turbine inertia together with the HVDC system capacitors. In this article, studies are carried out for a wind farm connected to an HVDC considering sudden load variations to compare and demonstrate the effectiveness of the control strategies. The stability of the HVDC system and the factors affecting it have not been investigated in this paper. Also, Mitra et al. [18] studied the integration of a DFIG-based offshore wind farm into a weak onshore grid through VSC-HVDC transmission system by using a new approach, known as the power-synchronization method. In this paper, onshore and offshore faults were considered and the fault-ride through techniques were presented; however, the impact of grid short-circuit power on the dc-link dynamic stability of the system was not discussed. In [19], a new configuration for the voltage source converter of the VSC-HVDC system was proposed to enhance the low-voltage ride-through capability and smooth power injection into the grid. This paper does not investigate the impact of grid short-circuit power and VSC-HVDC system parameters on stability of the VSC-HVDC system. In [20], a flywheel energy storage system was implemented for LVRT support of grid-connected VSC-HVDC-based offshore wind farms. The purpose of the mentioned study is to provide a reliable VSC-HVDC transmission system architecture between offshore wind farms and onshore grids.

Hence, according to the reviewed papers related to the VSC-HVDC-based wind farms, few analytical researches have been published regarding the system parameters and variables affecting the DC side stability. This paper deals with the modeling, control, and stability analysis of VSC-HVDC systems connected to offshore wind farms. The system under study comprises two 90 MW wind farms connected to the onshore grid via a VSC-HVDC transmission system, where each wind farm includes forty five 2 MW PMSG-based wind turbines. In this way, this study first dealt with the control of the offshore and onshore converters and then, mathematical modeling of the VSC-HVDC system and dc-link dynamics is presented. The offshore converter provides three-phase voltage with constant voltage and frequency and transmits the power from the wind farm to the VSC-HVDC system. The onshore converter regulates the dc-link voltage and exchanges reactive power with the onshore grid.

Next, the study examines the impacts of HVDC transmission line length and dc-voltage control bandwidth on the system stability by the modal analysis and time domain simulations. Also, it investigates the impact of onshore grid short-circuit power on the dc-link dynamic stability.

Hence, the main purpose of this paper is to study the stability of the dc-link dynamics in VSC-HVDC system and examine the impacts of the HVDC transmission line length and dc-voltage control bandwidth on the dc side stability using the modal analysis and time domain simulations.

2. Under study system layout

Figure 1 shows the layout of the study system that includes an onshore grid, transformers, converters, dc cables, and wind farms. In the system under study of Figure 1, two wind farms with a capacity of each 90 MW power generation are separately connected to VSC-HVDC transmission system. The HVDC

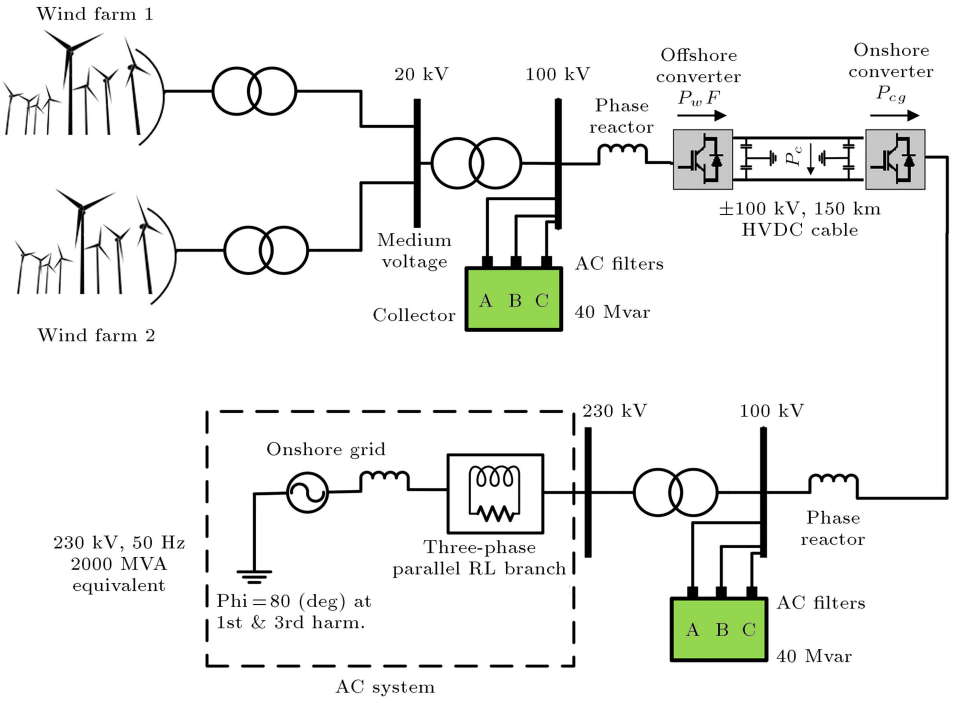

Figure 1. System layout under study.

transmission line parameters for this system are given in Appendix A (Table A.1). Each wind farm includes forty-five 2 MW full-scale converter wind turbines with 690 V rated voltage. Onshore grid is a 230 kV, 2000 MVA and 50 Hz AC system modeled by an ideal voltage source in series with R-L impedance, where the grid impedance angle at 50 Hz is equal to 80°.

There are several possible converter arrangements in an HVDC transmission system which can be divided into monopole and bipolar configurations based on the number of converters used at each terminal. In the monopole configuration, only one converter is used at each end of the network. Because of this characteristic, this method is more cost effective while the bipolar configuration employs two converters at each terminal. On the AC side, they are powered either by two different transformers, or by a transformer with two secondary windings. Monopolar configurations are divided into symmetric monopole, asymmetric monopole with metallic return, and asymmetric monopole with ground return configurations [21,22]. The system under study in this paper is based on symmetric monopole HVDC line configuration.

Among the different types of VSCs such as two-level, three-level, and Modular Multilevel Converter (MMC), the three-level VSCs with a switching frequency of 1350 Hz are used as the offshore and onshore converters. A 20 kV/100 kV transformer is used between the wind farm grid and offshore converter, and a 100 kV/230 kV transformer is used between the onshore converter and onshore grid. On the ac sides of both onshore and offshore converters, phase reactors with a size of 0.15 pu (0.0477 H) are used. In most cases like this, cross-linked polyethylene (XLPE) cables are used in VSC-HVDC transmission systems. XLPE has many benefits such as strong mechanical strength, flexibility, and low weight. The XLPE cable is mainly composed of conductor, insulation, water barrier, armoring, and outer sheath [23].

3. Offshore and onshore converters control

Generally, there are two main converters in the wind farm VSC-HVDC system known as offshore and onshore converters. By offshore converter, AC voltage with fixed amplitude and frequency is provided for the wind farm offshore grid. The offshore converter absorbs the power produced by offshore wind farms installed in the sea and transmits it into HVDC transmission system. At the end of HVDC line, active power is transferred to the ac onshore grid by the onshore converter.

3.1. Offshore converter controller

There are several ways to control the offshore converter. A simple method is direct control of AC voltage magnitude used in [24] and [25]. Figure 2 shows a block diagram of offshore converter control. In this figure, there is an AC voltage direct control loop keeping the amplitude and frequency of the AC bus voltage constant through modulation index (M).

This control method has some restrictions, such as

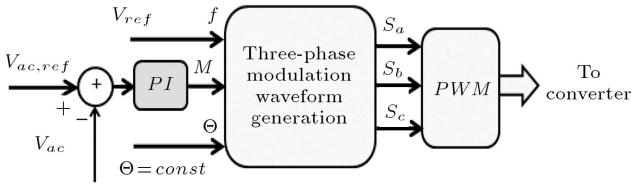

Figure 2. General block diagram of the Alternating Current (AC) voltage control by offshore converter.

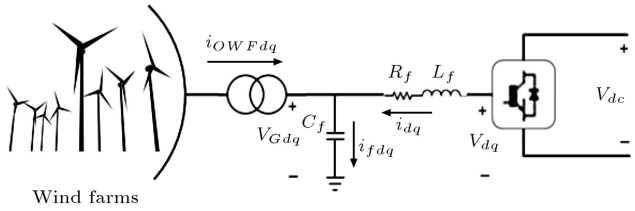

Figure 3. Wind farms connected to the offshore Alternating Current (AC) grid.

[26]: (1) There is no current loop control, thus limiting the converter current is difficult; (2) The controller parameters have a great impact on the behavior of the offshore converter, and in the event that the controller is not adjusted properly, there will be some transients at system response. In order to overcome these limitations, this article uses cascaded controllers including inner current control loop and outer voltage control loop. By the outer voltage control loop, the reference current for the inner current control loop is provided. The inner current control loop determines the converter output voltage in a manner that provides voltage with suitable frequency and amplitude for offshore AC grid. These controllers are of PI type and are implemented in the dq synchronous reference frame. Figure 3 shows the offshore converter and wind farm connected to the offshore AC grid.

Dynamic equations of the offshore converter in the dq-reference frame are given as follows:

$$C_f \frac{d}{dt} v_{Gd} = i_{OWFd} + i_d + \omega C_f v_{Gq}, \tag{1}$$

$$C_f \frac{d}{dt} v_{Gq} = i_{OWFq} + i_q - \omega C_f v_{Gd}, \tag{2}$$

$$L_f \frac{d}{dt} i_d = v_d - v_{Gd} - R_f i_d + \omega L_f i_q, \tag{3}$$

$$L_f \frac{d}{dt} i_q = v_q - v_{Gq} - R_f i_q - \omega L_f i_d, \tag{4}$$

where v_{Gd} and v_{Gq} represent the dq components of the offshore grid voltage; i_{OWFd} and i_{OWFq} denote the dq components of the offshore wind farm current; i_d and i_q are the dq components of offshore converter output current; v_d and v_q represent the dq components of the offshore converter output voltage; ω is the fundamental frequency of the offshore converter; and C_f and L_f represent the capacitance and inductance of the converter interface LC filter. In the following, the inner current and outer voltage control loops of the offshore converter are presented. Figure 4(a) and (b) show the inner dq current control loops of the offshore converter, where v_d and v_q as the offshore converter output voltages are given by:

$$v_d = v_{Gd} - \omega L_f i_q + k_{p1}(i_d^* - i_d) + k_{i1} \int (i_d^* - i_d), \tag{5}$$

$$v_q = v_{Gq} + \omega L_f i_d + k_{p1}(i_q^* - i_q) + k_{i1} \int (i_q^* - i_q), \tag{6}$$

where k_{i1} and k_{p1} are the PI controller parameters.

It is noted that in Figure 4(a) and (b), the terms v_{Gd}, $\omega L i_q$ and v_{Gq} and $\omega L i_d$ act as disturbances; thus, to improve the dynamics of the current control loops, they are compensated by the feedforward terms.

Also, Figure 5(a) and (b) depict the outer dq voltage control loops of the offshore where $\alpha/(s+\alpha)$ is the closed-loop Transfer Function (TF) of the inner current loop. Hence, α is the closed-loop bandwidth of the converter inner current control loop. α is a design parameter and is roughly selected as $\alpha << \omega_{sw}$, where ω_{sw} denotes the conveter switching frequency. For the system under study, α is selected equal to $2\pi \times 100$ rad/sec or 100 Hz. The dq voltage controllers provide the reference currents i_d^* and i_q^* as given below:

$$i_d^* = -i_{OWFd} - \omega C_f v_{Gq} + k_{p2}(v_{Gd}^* - v_{Gd}) + k_{i2} \int (v_{Gd}^* - v_{Gd}), \tag{7}$$

$$i_q^* = -i_{OWFq} + \omega C_f v_{Gd} + k_{p3}(v_{Gq}^* - v_{Gq}) + k_{i3} \int (v_{Gq}^* - v_{Gq}), \tag{8}$$

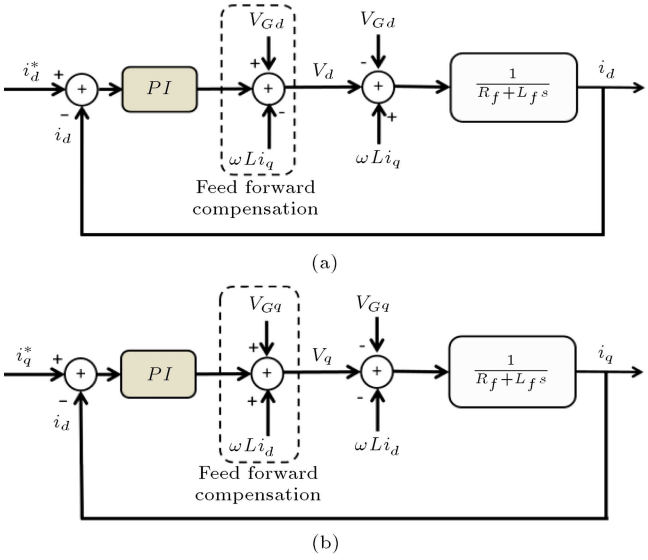

Figure 4. Inner current control loop of offshore converter: (a) d-axis, (b) q-axis.

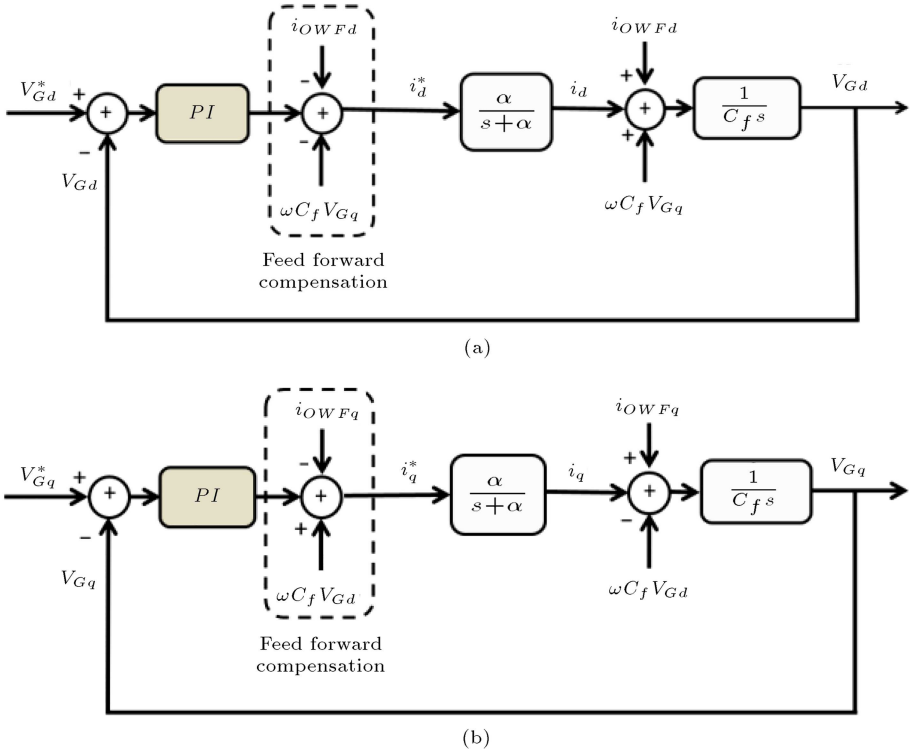

Figure 5. Outer voltage control loops of the offshore converter: (a) d-axis, (b) q-axis.

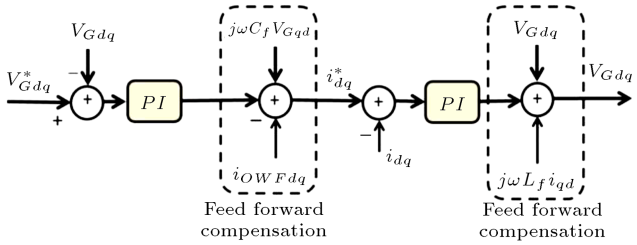

Figure 6. Overall control block diagram of the offshore converter.

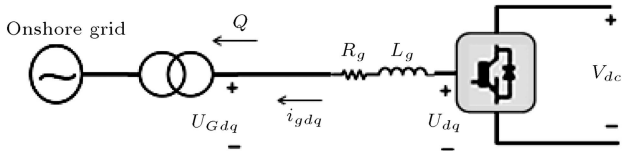

Figure 7. Onshore converter circuit model connected to the onshore Alternating Current (AC) grid.

where k_{i2}, k_{i3}, k_{p2}, and k_{p3} are the parameters associated with PI controllers.

In the control loops of Figure 5(a) and (b), the terms i_{OWFd}, $\omega C_f v_{Gq}$, i_{OWFq} and $\omega C_f v_{Gd}$ act as disturbances, and similar to Figure 4, they are compensated by the feedforward terms.

More details for the design of the inner and outer loop controllers are available in [27]. Figure 6 depicts the overall control block diagram of the offshore converter.

3.2. Onshore converter controller

Under normal operating conditions, the purpose of the onshore converter control is the dc-link voltage regulation that enables power transmission from the wind farm to the grid. Onshore converter can also exchange reactive power with the onshore grid. Figure 7 shows the onshore converter connected to the onshore grid through the interface R_g-L_g filter.

The dynamic model of the onshore converter in the dq synchronous reference frame is given as follows:

$$U_d = U_{Gd} - \omega L_g i_{gq} + L_g\left(\frac{d i_{gd}}{dt}\right) + R_g i_{gd}, \tag{9}$$

$$U_q = U_{Gq} + \omega L_g i_{gd} + L_g\left(\frac{d i_{gq}}{dt}\right) + R_g i_{gq}, \tag{10}$$

where U_q and U_d are the converter output voltages; U_{Gd} and U_{Gq} are onshore grid voltages; i_{gd} and $i_{gq}$are converter output currents; L_g and R_g represent the interface filter inductance and resistance; and ω is the onshore grid frequency. To facilitate the controller design, the d-axis is adapted to the onshore grid AC voltage and q-axis is 90° ahead of the d-axis; thus, $U_{Gd} = U_G$ and $U_{Gq} = 0$ and task of i_{gd} is the DC-link voltage regulation and task of i_{gq} is regulation of reactive power injected to the onshore grid. Similar to the offshore converter, the onshore converter is controlled by the cascaded control approach comprising the inner current control loops and outer DC-link and reactive power control loops. Figure 8(a) and (b) show the onshore converter inner current control loops.

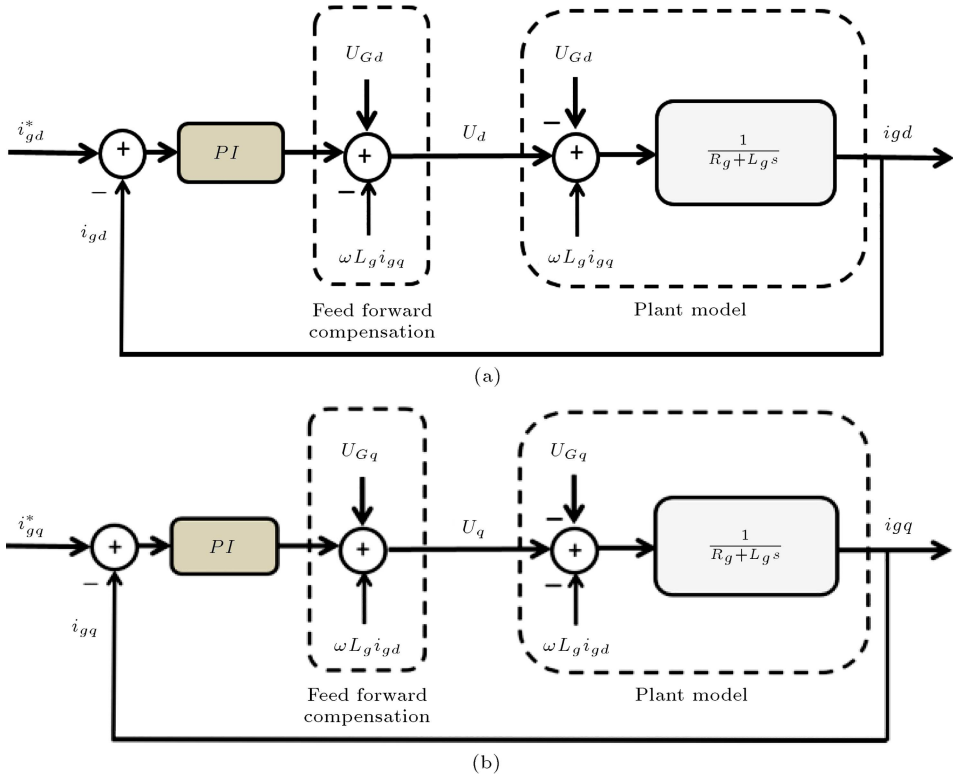

Figure 8. Inner current control loops of the onshore converter: (a) d-axis, (b) q-axis.

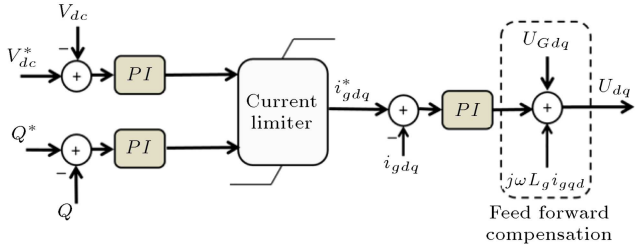

Figure 9. Overall block diagram of the onshore converter control.

Also, Figure 9 depicts the overall control scheme of the onshore converter comprising the outer DC-link voltage and reactive power loops.

Considering Figure 9, the dq reference currents i^*_{gd} and i^*_{gq} are given as:

$$i^*_{gd} = -k_{pdc1}(v^*_{dc} - v_{dc}) - k_{idc1}\int (v^*_{dc} - v_{dc}), \qquad (11)$$

$$i^*_{gq} = -k_{pdc2}(Q^* - Q) - k_{idc2}\int (Q^* - Q), \qquad (12)$$

where k_{pdc1}, k_{pdc2}, k_{idc1}, and k_{idc2} are the parameters associated with the PI controllers.

4. Stability analysis of VSC-HVDC grid and onshore converter controller

This section deals with the stability analysis of the system on the DC side and DC-link voltage controller design for the onshore converter. Since the controller parameters affect the DC grid dynamics of the HVDC system, after controller design, dynamic analysis of the DC grid is also performed. In this way, state equations of the HVDC system are extracted and impacts of the DC-link control bandwidth, length of HVDC transmission line, and short-circuit power of the onshore AC grid on the stability and performance of the HVDC system are examined.

Figure 10 shows the structure of the VSC-HVDC system used in the system under study in Figure 1, which is a symmetrical monopole VSC-HVDC system. For analysis and modeling of the DC-side dynamics, the equivalent model shown in Figure 11 can be used which is an asymmetric monopole model with the ground return. In Figure 10, cables of the HVDC transmission system are modeled by the π model. Each onshore or offshore converter has C_1 and C_2 capacitors on the DC side. An onshore converter through the inductive filter with L_g inductance and R_g resistance is connected to the AC grid. Also, the offshore converter is connected to the wind farm through LC filter. In Figure 11, $P_1 = P_{t1}/2$ and $P_2 = P_{t2}/2$, where according to Figure 10, P_{t1} and P_{t2} are the offshore grid output power and onshore grid input power, respectively.

4.1. State equations of the open-loop VSC-HVDC system

In order to extract state equations and modal analysis

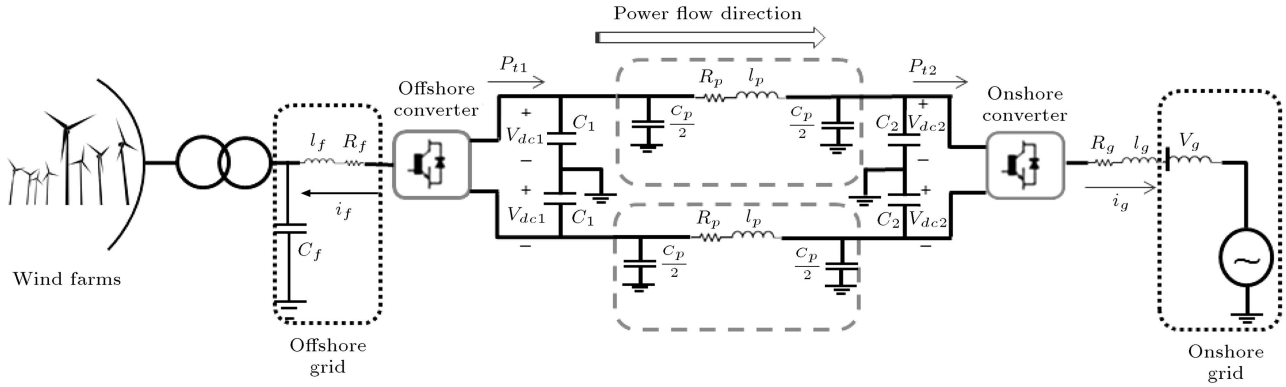

Figure 10. Symmetric monopole VSC-HVDC system with a detailed DC-transmission link.

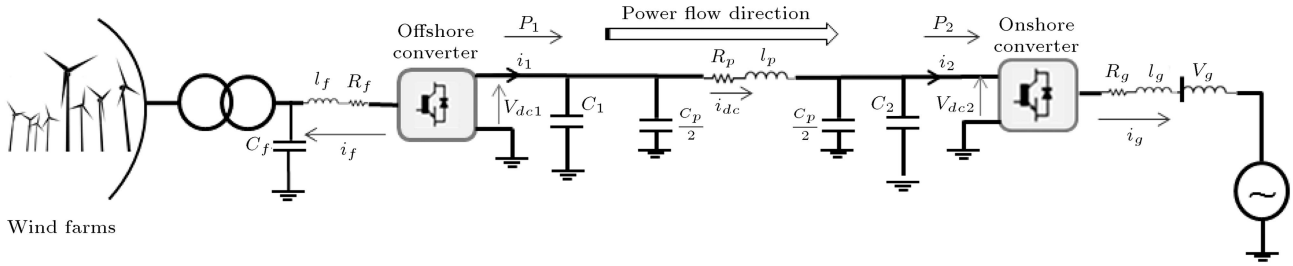

Figure 11. Asymmetric equivalent model of the VSC-HVDC system given in Figure 10.

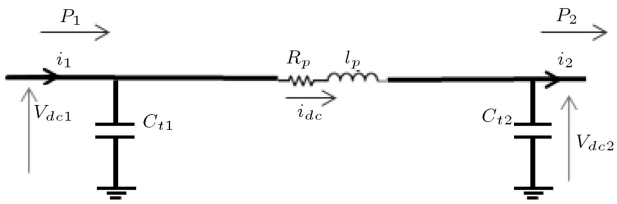

Figure 12. Simplified equivalent model of the VSC-HVDC system.

of the HVDC system, the equivalent model of the DC-transmission link given in Figure 11 is considered. Considering Figure 11, simplified model of the VSC-HVDC system of Figure 11 is obtained as depicted in Figure 12, where $C_{t1} = C_1 + C_p/2$ and $C_{t2} = C_2 + C_p/2$. According to Figure 12, state equations of the DC side are given by:

$$C_{t1}\frac{dV_{dc1}}{dt} = i_1 - i_{dc},$$

$$L_p\frac{di_{dc}}{dt} = -R_p\, i_{dc} + V_{dc1} - V_{dc2},$$

$$C_{t2}\frac{dV_{dc2}}{dt} = i_{dc} - i_2, \tag{13}$$

where $i_1 = \frac{P_1}{V_{dc1}}$ and $i_2 = \frac{P_2}{V_{dc2}}$. By linearizing Eq. (13) around operating point, we have:

$$C_{t1}\frac{d\Delta V_{dc1}}{dt} = \Delta i_1 - \Delta i_{dc},$$

$$L_p\frac{d\Delta i_{dc}}{dt} = -R_p\,\Delta i_{dc} + \Delta V_{dc1} - \Delta V_{dc2},$$

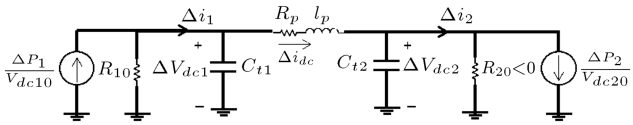

Figure 13. Small signal model of the VSC-HVDC system.

$$C_{t2}\frac{d\Delta V_{dc2}}{dt} = \Delta i_{dc} - \Delta i_2, \tag{14}$$

where Δ denotes the small deviation around the operating point. In Eq. (14), Δ_{i1} and Δ_{i2} are given as $\Delta i_1 = \frac{\Delta P_1}{V_{dc10}} - \frac{P_{10}}{V_{dc20}^2}\Delta V_{dc1}$ and $\Delta i_2 = \frac{\Delta P_2}{\Delta V_{dc20}} - \frac{P_{20}}{V_{dc20}^2}\Delta V_{dc2}$. Replacing Δ_{i1} and Δ_{i2} with the corresponding expressions, the state equations of Eq. (14) can be given as follows:

$$C_{t1}\frac{d\Delta V_{dc1}}{dt} = \frac{\Delta P_1}{v_{dc10}} - \frac{P_{10}}{v_{dc10}^2}\Delta V_{dc1} - \Delta i_{dc},$$

$$L_p\frac{d\Delta i_{dc}}{dt} = -R_p\,\Delta i_{dc} + \Delta V_{dc1} - \Delta V_{dc2},$$

$$C_{t2}\frac{d\Delta V_{dc2}}{dt} = \Delta i_{dc} - \frac{\Delta P_2}{\Delta V_{dc20}} + \frac{P_{20}}{V_{dc20}^2}\Delta V_{dc2}. \tag{15}$$

From Eq. (15), the equivalent small signal model of the VSC-HVDC system is obtained, as depicted in Figure 13, where $R_{10} = \frac{V_{dc20}^2}{P_{10}} > 0$ and $R_{20} = -\frac{V_{dc20}^2}{P_{20}} < 0$.

Dynamic equations of Eq. (15) can be written in the form of $\Delta x^{\bullet} = A\Delta x + B\Delta u, \Delta y = C\Delta x$, where

$$G(s) = \frac{\Delta V_{dc2}}{-\Delta P_2} = \frac{C_t^{-1} V_{dc2,0}^{-1} [s^2 + (\alpha_1 + \alpha_4)s + (\alpha_3 + \alpha_1\alpha_4)]}{s^3 + (\alpha_1 + \alpha_2 + \alpha_4)s^2 + [2\alpha_3 + \alpha_1\alpha_4 + \alpha_1\alpha_2 + \alpha_2\alpha_4]s + (\alpha_1\alpha_3 + \alpha_2\alpha_3 + \alpha_1\alpha_2\alpha_4)}. \quad (16)$$

Box I

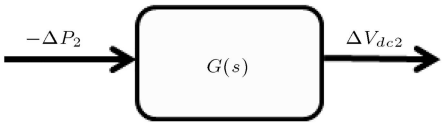

Figure 14. Open loop transfer function of the VSC-HVDC system.

A is a 3×3 matrix and $\Delta x = [\Delta V_{dc1} \ \Delta i_{dc} \ \Delta V_{dc2}]^T$, $\Delta u = [\Delta P_1 \ \ \Delta P_2]^T$, and $\Delta y = \Delta V_{dc2}$.

In the mentioned state equations of Eq. (15), ΔP_2 is the control input used to regulate V_{dc2} at the desired value and ΔP_1 also acts as the disturbance. From Eq. (15), the open-loop transfer function $G(s)$ from $-\Delta P_2$ to ΔV_{dc2} is given by Eq. (16) as shown in Box I. Transfer function of Eq. (16) can be represented, as depicted in Figure 14.

Similarly, the transfer function from ΔP_1 to ΔV_{dc2} can be written in Eq. (17) as shown in Box II. In Eqs. (16) and (17), $\alpha_1 = \frac{1}{C_t R_{10}}$, $\alpha_2 = \frac{1}{C_t R_{20}}$, $\alpha_3 = \frac{1}{L_p C_t}$, and $\alpha_4 = \frac{R_p}{L_p}$. Considering Figure 10 and neglecting the onshore converter losses, the power injected to the onshore grid is given by:

$$P_{t2} = \frac{3}{2} V_{gd} i_{gd}. \quad (18)$$

In Figure 11, $P_2 = P_{t2}/2$ and thus we have:

$$\Delta P_2 = \frac{1}{2}\frac{3}{2} V_{gd} \Delta i_{gd}. \quad (19)$$

To obtain ΔP_2 in Eq. (19), it is assumed that the onshore grid is sufficiently stiff and $\Delta V_{gd} \approx 0$. According to Eqs. (16) and (19) and Figure 14, the closed-loop control system of the DC-link voltage on the onshore side is obtained, as depicted in Figure 15.

The transfer function $G(s)$ in Figure 15 is the one presented in Eq. (16). If the impacts of the HVDC transmission line dynamics on the DC-link dynamics of the onshore converter are ignored, the transfer function $G(s)$ changes into the simple form of Eq. (20):

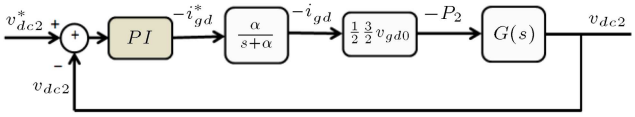

Figure 15. Closed-loop control system of the DC-link voltage.

$$G_1(s) = \frac{V_{dc2}(s)}{-P_2(s)} = \frac{1}{C_t V_{dc20} s}. \quad (20)$$

4.2. DC-link voltage control design

As previously mentioned, the task of the onshore converter is regulation of the DC-link voltage at the reference value and transferring the wind farms power to the onshore AC grid. There are two approaches to the selection of the DC-link controller parameters:

a) Considering the simple transfer function of Eq. (20) without taking the HVDC transmission line dynamics into account;

b) Considering the whole system dynamics and using the transfer function of Eq. (16).

Since the first approach is easier to use, DC-link controller is designed in this section based on the simple transfer function of Eq. (20). Figure 16 shows the closed-loop block diagram of the DC-link voltage control on the onshore converter side using the simple transfer function.

Following the selection of the DC-link controller parameters, stability and performance of the whole HVDC-side dynamics are investigated for the mentioned controller.

In Figure 16, since the inner current control dynamics is much faster than the outer DC-link voltage

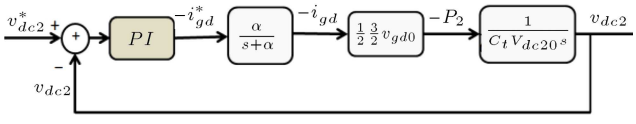

Figure 16. Simplified block diagram of the DC-link voltage control by the onshore side converter.

$$D(s) = \frac{\Delta V_{dc2}}{\Delta P_1} = \frac{\alpha_3 C_t^{-1} V_{dc2,0}^{-1}}{s^3 + (\alpha_1 + \alpha_2 + \alpha_4)s^2 + [2\alpha_3 + \alpha_1\alpha_4 + \alpha_1\alpha_2 + \alpha_2\alpha_4]s + (\alpha_1\alpha_3 + \alpha_2\alpha_3 + \alpha_1\alpha_2\alpha_4)}. \quad (17)$$

Box II

control, the term $\alpha/(s+\alpha)$ can be replaced with 1. Consequently, the closed-loop transfer function in Figure 16 can be described by:

$$\frac{V_{dc2}}{V^*_{dc2}} = \frac{2\zeta\omega_n s + \omega_n^2}{s^2 + 2\zeta\omega_n s + \omega_n^2}, \tag{21}$$

where:

$$\omega_n^2 = \frac{3}{4C_t v_{dc20}} v_{gd}\, k_{idc},$$

$$2\zeta\omega_n = \frac{3}{4C_t v_{dc20}} v_{gd}\, k_{pdc}, \tag{22}$$

where k_{pdc} and k_{idc} are the PI controller parameters. By selecting $\zeta = 0.7$ and $\omega_n = 85$ rad/sec, the controller parameters $k_{pdc} = \frac{8\zeta\omega_n C_t v_{dc20}}{3v_{gd}}$, and $k_{idc} = \frac{4\omega_n^2 C_t v_{dc20}}{3v_{gd}}$, for the system under study with parameters of Appendix A (Table A.1) and 100 km HVDC transmission line are obtained as $k_{pdc} = 0.011$ and $k_{idc} = 0.69$.

4.3. Small signal stability analysis of the VSC-HVDC system

In this section, the impact of DC-link controller and DC transmission line length on the HVDC system stability is investigated. State equations of the HVDC side dynamics considering the outer DC-link voltage controller and inner d-axis current dynamics are given by:

$$C_{t1}\frac{d\Delta V_{dc1}}{dt} = \frac{\Delta P_1}{V_{dc10}} - \frac{\Delta V_{dc1}}{R_{10}} - \Delta i_{dc},$$

$$L_p\frac{d\Delta i_{dc}}{dt} = -R_p\Delta i_{dc} + \Delta V_{dc1} - \Delta V_{dc2},$$

$$C_{t2}\frac{d\Delta V_{dc2}}{dt} = \Delta i_{dc} - \frac{\Delta P_2}{V_{dc20}} - \frac{\Delta V_{dc2}}{R_{20}},$$

$$\frac{d\Delta i_{gd}}{dt} = -\alpha\Delta i_{gd} + \alpha\Delta i^*_{gd},$$

$$\Delta x^{\bullet}_{dc} = \Delta V^*_{dc2} - \Delta V_{dc2}, \tag{23}$$

where:

$$\Delta P_2 = \frac{3}{4} V_{gd}\,\Delta i_{gd},$$

$$\Delta i^*_{gd} = -k_{pdc}(\Delta V^*_{dc2} - \Delta V_{dc2}) - k_{idc}\int(\Delta V^*_{dc2} - \Delta V_{dc2})dt. \tag{24}$$

By substituting Eq. (24) into Eq. (23), we have:

$$C_{t1}\frac{d\Delta V_{dc1}}{dt} = \frac{\Delta P_1}{V_{dc10}} - \frac{\Delta V_{dc1}}{R_{10}} - \Delta i_{dc},$$

$$L_p\frac{d\Delta i_{dc}}{dt} = -R_p\Delta i_{dc} + \Delta V_{dc1} - \Delta V_{dc2},$$

$$C_{t2}\frac{d\Delta V_{dc2}}{dt} = \Delta i_{dc} - \frac{3V_{gd0}}{4V_{dc20}}\Delta i_{gd} - \frac{\Delta V_{dc2}}{R_{20}},$$

$$\frac{d\Delta i_{gd}}{dt} = -\alpha\Delta i_{gd} - \alpha k_{pdc}\Delta V^*_{dc2} + \alpha k_{pdc}\Delta V_{dc2} - \alpha k_{idc}\Delta x_{dc},$$

$$\frac{d\Delta x_{dc}}{dt} = \Delta V^*_{dc2} - \Delta V_{dc2}, \tag{25}$$

where x_{dc} is the state variable related to the DC-link controller and α is the closed-loop bandwidth of the inner current control loop. State equations of Eq. (25) are in the form of $\Delta x^{\bullet} = A\Delta x + B\Delta u$ where A is a 5×5 state matrix and the state vector (Δx) and input (Δu) are $\Delta x^{\bullet} = [\Delta V_{dc1}\ \Delta i_{dc}\ \Delta V_{dc2}\ \Delta i_{gd}\ \Delta x_{dc}]^T$, $\Delta u = [\Delta P_1\ \Delta V^*_{dc2}]^T$.

Modal analysis shows that the dc-link control bandwidth and HVDC transmission line affect the system dynamics. Modal analysis results for the different DC-link control bandwidths and HVDC transmission line lengths briefly are presented in Table 1.

It is clear that at the line length equal to 100 km, the DC-link voltage of the system is stable at all DC-link control bandwidths from 10 to 50 Hz. The results of the analysis show that the stability of the system is highly affected at the lower bandwidths. Also, modal analysis shows that increasing the line length while keeping the dc-link control bandwidth constant results in the modes with lower stability margin. Figure 17 shows the bode diagram of the DC-link control loop gain at 150 km transmission line length and for DC-link control bandwidths of 10 and 20 Hz. According to Figure 17, at 150 km line length and for DC-link control bandwidths of 10 and 20 Hz, the phase margin is negative and the closed-loop DC-link dynamics is unstable.

5. Simulation results

This section deals with the time domain simulation of the system under study in Figure 1. The effects of the HVDC transmission line length and DC-link control closed-loop bandwidth on the stability and performance of the HVDC system and the impact of short-circuit power of the onshore AC grid on the DC-link voltage dynamics are examined by simulation results.

5.1. Effects of the HVDC transmission line length and DC-link control closed-loop bandwidth on the HVDC system

Figures 18 and 19 show the offshore and onshore converter responses at $V_w = 12$ m/s, transmission line length of 100 km, and DC-link control bandwidth of 50 Hz. Figure 18 shows the output real power of the offshore converter (transferred to the onshore converter), reactive power exchanged by offshore converter, and DC-link voltage of the offshore converter

Table 1. Modal analysis for different DC-link controller bandwidth and HVDC transmission line lengths.

Bandwidth	Line length	Eigenvalues (100×)	PM (deg)	GM (db)	Stability
10 Hz	100 km	$-0.0995 \pm 3.4738i$; $-0.0039 \pm 0.0013i$; -1.2566	89.4	88.4	Stable
	150 km	$-0.1002 \pm 2.7489i$; $0.0005 \pm 0.0041i$; -1.2566	-0.334	4.05	Unstable
20 Hz	100 km	$-0.0995 \pm 3.4738i$; $-0.0039 \pm 0.0072i$; -2.5132	83.6	84.5	Stable
	150 km	$-0.1002 \pm 2.7489i$; $0.0005 \pm 0.0083i$; -2.5132	0.0175	-1.75	Unstable
30 Hz	100 km	$-0.0995 + 3.4738i$; $-0.0995 - 3.4738i$ $-0.0039 + 0.0116i$; $-0.0039 - 0.0116i$ -3.7698	53.6	75.9	Stable
	150 km	$-0.1001 + 2.8222i$; $-0.1001 - 2.8222i$ $-0.0001 + 0.0124i$; $-0.0001 - 0.0124i$ -3.7698	0.335	73.1	Stable
40 Hz	100 km	$-0.0995 \pm 3.4739i$; $-0.0039 \pm 0.0158i$; -5.0264	39.8	70.1	Stable
	150 km	$-0.1001 \pm 2.8222i$; $-0.0002 \pm 0.0166i$; -5.0264	0.598	67.6	Stable
50 Hz	100 km	$-0.0995 \pm 3.4739i$; $-0.0039 \pm 0.0200i$; -6.2830	31.9	65.9	Stable
	150 km	$-0.1001 \pm 2.8222i$; $-0.0003 \pm 0.0207i$; -6.2830	0.832	63.4	Stable

V_{dc1}. According to Figure 18(a), 145 MW active power is transferred to the HVDC system by the offshore converter. Figure 18(b) specifies that the reactive power exchanged between the converter and offshore AC grid is close to zero. DC-link voltage of offshore converter compared to the neutral point fixed at 1 pu is shown in Figure 18(c).

Figure 19 shows the DC-link voltage of the onshore converter V_{dc2} and output active power of the onshore converter injected into the grid. According

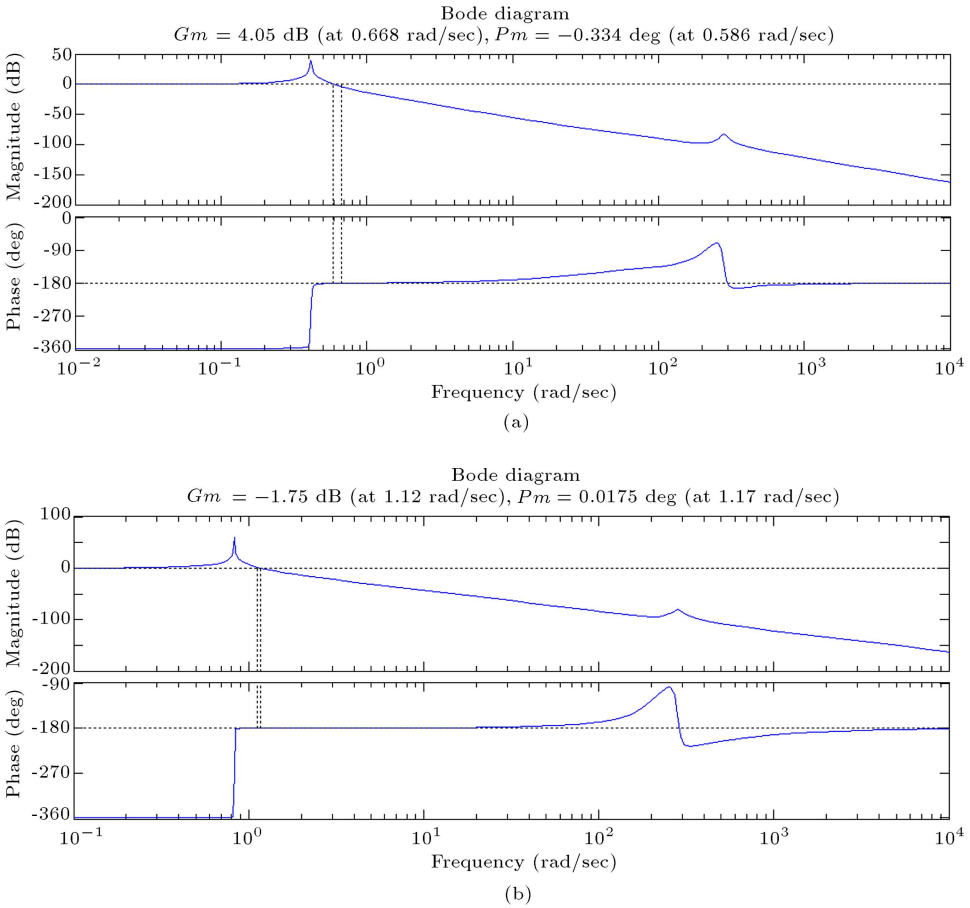

Figure 17. Bode diagram of the system under study with 150 km line length for two different DC-link control bandwidths: (a) 10 Hz and (b) 20 Hz.

to Figure 19(b), 130 MW active power is delivered to the onshore converter and thus, there is 15 MW power loss in the HVDC transmission line. As can be seen in Figure 19(a), the DC-link voltage in the onshore converter is stable and has been set to its reference value. According to Figures 18 and 19, the system response is stable and this is in agreement with the modal analysis results.

Figure 20 shows the DC-link voltage of the onshore side for different values of DC-link voltage control bandwidths and at a transmission line length of 150 km. It is clear that for the DC-link bandwidths of 10 Hz and 20 Hz, the system is unstable, as mentioned in the modal analysis.

5.2. Effects of onshore grid short-circuit power on the DC link voltage dynamics

In the simulation results of Figures 18–20, the short-circuit power (S_{sc}) of the onshore grid was considered equal to 2000 MVA. In this section, the HVDC line length is considered 100 Km and the DC-link control bandwidth is selected equal to 50 Hz; then, the effect of onshore grid short-circuit power (S_{sc}) on the DC-link stability is examined. Figure 21 shows the DC-link voltage on the onshore side at four different values of onshore grid short-circuit power, i.e., 2000 MVA, 1000 MVA, 500 MVA, and 200 MVA.

As depicted in Figure 21, by weakening the AC onshore grid, the DC-link dynamics moves toward the unstable state. According to Figure 21, at S_{sc} = 500 and 200 MVA, the DC-link voltage response is oscillatory and unstable.

6. Conclusion

This study dealt with the studying, modeling, and control of the VSC-HVDC system connected to offshore wind farms and addressed some issues regarding the factors affecting the stability of the system under study. In this way, theoretical and mathematical expressions regarding the control and modeling of the VSC-HVDC connected wind farm were presented. Then, by the modal and frequency response analysis and time domain simulations, the impacts of the DC-link control bandwidth, the HVDC line length, and the onshore grid short-circuit power on the system stability were examined. Consequently, by increasing the HVDC line length and reducing the DC-link voltage bandwidth,

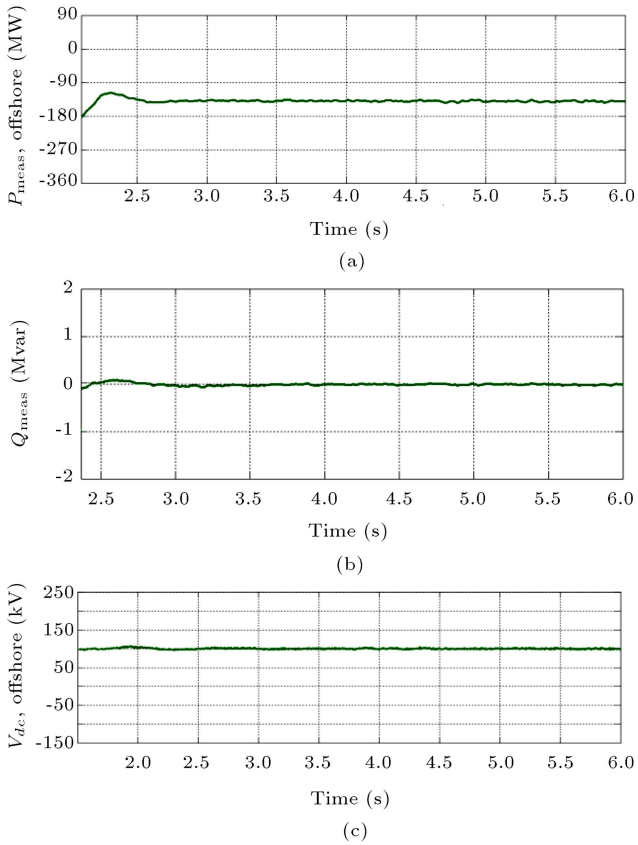

Figure 18. Waveforms related to HVDC system performance and offshore converter: (a) Offshore converter output active power, (b) reactive power exchanged between the converter and offshore AC grid, and (c) DC-link voltage of offshore converter compared to the neutral point.

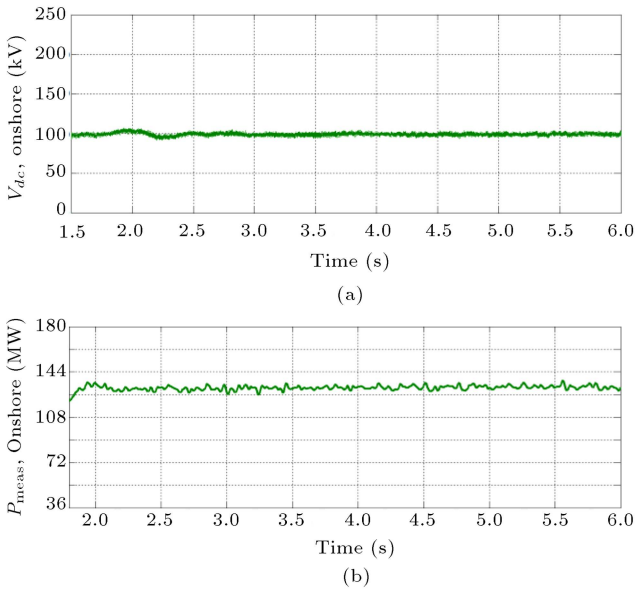

Figure 19. Waveforms related to HVDC system performance and onshore converter: (a) Onshore DC voltage and (b) active power delivered to the onshore converter.

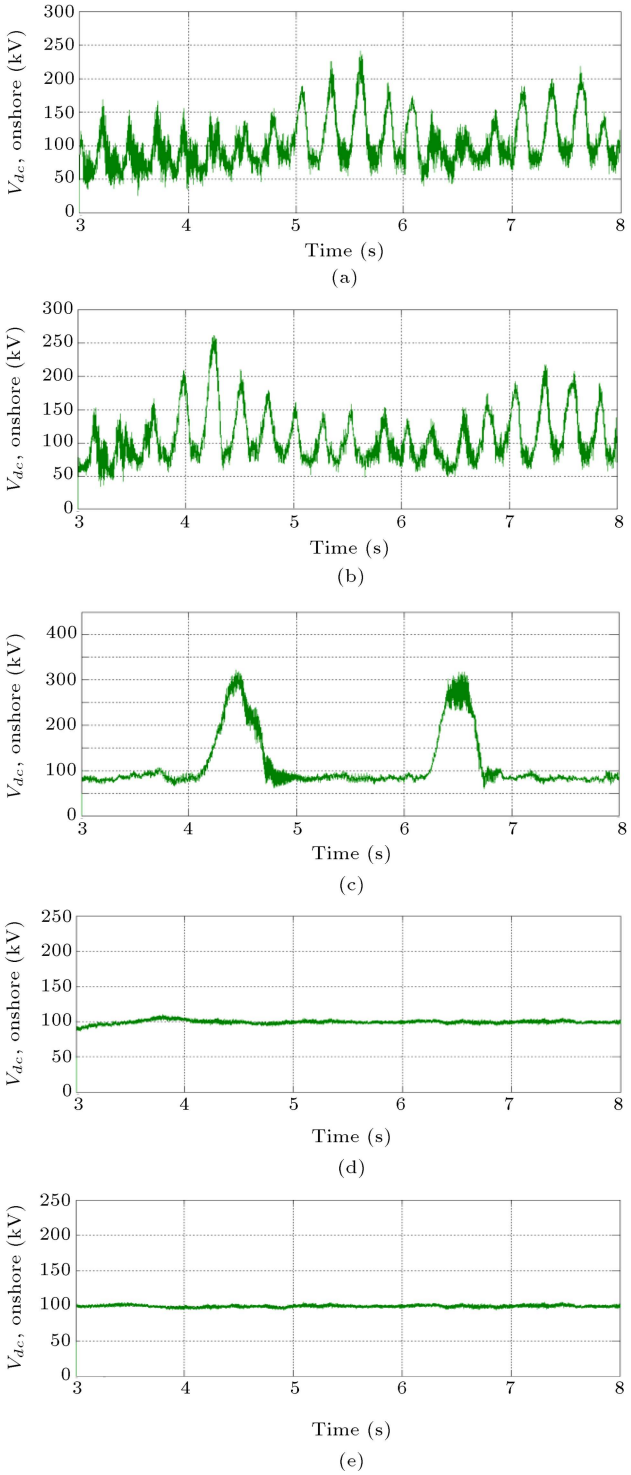

Figure 20. Effects of controller coefficients variations with bandwidth changes on the DC-link voltage: (a) 10 Hz, (b) 20 Hz, (c) 30 Hz, (d) 40 Hz, and (e) 50 Hz.

the system modes and responses moved toward the unstable state. Also, at a HVDC line length of 150 Km, the system responses were unstable at DC-link control bandwidths of 10 Hz and 20 Hz. In the case of weak AC onshore grid, the DC-link dynamics may become unstable. In this paper, the effect of grid short-circuit

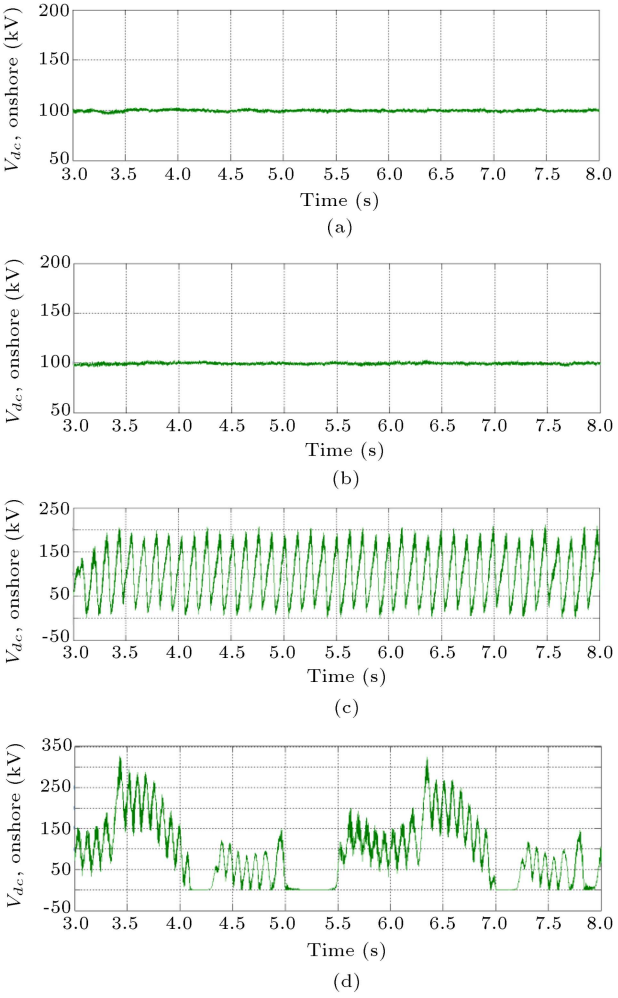

Figure 21. Effects of onshore grid short-circuit power (S_{sc}) on DC-link voltage response: (a) 2000 MVA, (b) 1000 MVA, (c) 500 MVA, and (d) 200 MVA.

power on the DC-link voltage response was studied. It was shown that the response of the system under study was unstable when the short-circuit power of the onshore grid was 500 MVA or less.

References

1. Egea-Alvarez, A., Bianchi, F., Junyent-Ferré, A., et al. "Voltage control of multiterminal VSC-HVDC transmission systems for offshore wind power plants: Design and implementation in a scaled platform", *IEEE Transactions on Industrial Electronics*, **60**(6), pp. 2381–2391 (2013).
2. 2017 European Statistics. EWEA Std. [Online]. Available: http://www.ewea.org/Statistics. Accessed 15 February 2018.
3. The European Offshore Wind Industry-Key Trends and Statistics 2016 (2017). https://windeurope.org/about-wind/statistics/offshore/european-offshore-wind-industry-key-trends-and-statistics-2016. Accessed 26 January 2017.
4. Raza, A., Dianguo, X., Xunwen, S., et al. "A novel multiterminal VSC-HVdc transmission topology for offshore wind farms", *IEEE Transactions on Industry Applications*, **53**(2), pp. 1316–1325 (2017).
5. Haileselassie, T.M. "Control, dynamics and operation of multi-terminal VSC-HVDC transmission systems", Doctoral thesis, NTNU University (2012).
6. Prabhu, N.A., Latha, R., Sankaran, K., et al. "Impact of knowledge management on offshore software development: An exploratory study", In *Advanced Computing (ICoAC), 2011 Third International Conference on*, pp. 121–128, IEEE (2011).
7. Li, Q. and Wang, H. "Two-stage simulation optimization for optimal development of offshore wind farm under wind uncertainty", In *Proceedings of the 2016 Winter Simulation Conference*, pp. 2891–2902, IEEE Press (2016).
8. Chodura, P., Gibescu, M., Kling, W.L., et al. "Investigation of the impact of embedded VSC-HVDC active and reactive power control on power system stability", In *PowerTech, 2015 IEEE Eindhoven*, pp. 1–6, IEEE (Jun., 2015).
9. Erlich, I., Shewarega, F., and Winter, W. "A method for incorporating VSC-HVDC into the overall grid voltage-reactive power control task", In *Power Systems Computation Conference (PSCC)*, IEEE, pp. 1–7, (Jun., 2016).
10. Liu, Y. and Chen, Z. "Voltage sensitivity based reactive power control on VSC-HVDC in a wind farm connected hybrid multi-infeed HVDC system", In *PowerTech (POWERTECH), 2013 IEEE Grenoble*, IEEE, pp. 1–6, (Jun., 2013).
11. Wei, C.Z., Mou, M., An, W., et al. "Optimization of reactive power and voltage for hybrid AC/VSC-HVDC system", *12th IET International Conference on AC and DC Power Transmission (ACDC 2016)* (2016).
12. Perveen, R., Kishor, N., and Mohanty, S.R. "Offshore wind farm development: Present status and challenges", *Renewable and Sustainable Energy Reviews*, **29**, pp. 780–792 (2014).
13. Bahrman, M.P. and Johnson, B.K. "The ABCs of HVDC transmission technologies", *IEEE Power and Energy Magazine*, **5**(2), pp. 32–44 (2007).
14. Müller, H.K., Torbaghan, S.S., Gibescu, M., et al. "The need for a common standard for voltage levels of HVDC VSC technology", *Energy Policy*, **63**, pp. 244–251 (2013).
15. Muyeen, S.M., Takahashi, R., and Tamura, J. "Operation and control of HVDC-connected offshore wind farm", *IEEE Transactions on Sustainable Energy*, **1**(1), pp. 30–37 (2010).
16. Kunjumuhammed, L.P., Pal, B.C., Gupta, R., et al. "Stability analysis of a PMSG-based large offshore wind farm connected to a VSC-HVDC", *IEEE Transactions on Energy Conversion*, **32**(3), pp. 1166–1176 (2017).

17. Li, Y., Xu, Z., ϕstergaard, J., and Hill, D.J. "Coordinated control strategies for offshore wind farm integration via VSC-HVDC for system frequency support", *IEEE Transactions on Energy Conversion*, **32**(3), pp. 843–856 (2017).

18. Mitra, P., Zhang, L., and Harnefors, L. "Offshore wind integration to a weak grid by VSC-HVDC links using power-synchronization control: A case study", *IEEE Transactions on Power Delivery*, **29**(1), pp. 453–461 (2014).

19. Moawwad, A., El Moursi, M.S., and Xiao, W. "Advanced fault ride-through management scheme for VSC-HVDC connecting offshore wind farms", *IEEE Transactions on Power Systems*, **31**(6), pp. 4923–4934 (2016).

20. Daoud, M.I., Massoud, A.M., Abdel-Khalik, A.S., et al "A flywheel energy storage system for fault ride through support of grid-connected VSC HVDC-based offshore wind farms", *IEEE Transactions on Power Systems*, **31**(3), pp. 1671–1680 (2016).

21. De Boeck, S., Tielens, P., Leterme, W., et al. "Configurations and earthing of HVDC grids", In *Power and Energy Society General Meeting (PES)*, pp. 1–5 (Jul., 2013).

22. Pinto, R.T. and La Seta, P., *Dynamics and Control of VSC-Based HVDC Systems: A Practical Approach to Modeling and Simulation*, LAP Lambert Academic Publishing (2012).

23. Vrana, T.K. and Energi, S. "Review of HVDC component ratings: XLPE cables and VSC converters", In *Energy Conference (ENERGYCON), 2016 IEEE International*, pp. 1–6 (Apr., 2016).

24. Xu, L. and Andersen, B.R. "Grid connection of large offshore wind farms using HVDC", *Wind Energy*, **9**(4), pp. 371–382 (2006).

25. Xiang, D., Ran, L., Bumby, J.R., et al. "Coordinated control of an HVDC link and doubly fed induction generators in a large offshore wind farm", *IEEE Transactions on Power Delivery*, **21**(1), pp. 463–471 (2006).

26. Olguin, R.E.T. "Grid integration of offshore wind farms using hybrid hvdc transmission: Control and operational characteristics", Doctoral thesis, NTNU University (2013).

27. Chinchilla, M., Arnaltes, S., and Burgos, J.C. "Control of permanent-magnet generators applied to variable-speed wind-energy systems connected to the grid", *IEEE Transactions on Energy Conversion*, **21**(1), pp. 130–135 (2006).

Appendix A

Parameters related to the system under study of Figure 1 are given in Table A.1.

Table A.1. Parameters related to the system under study shown in Figure 1.

Section	Parameter	Amount	Unit
Wind farms	Number of wind farms	2	...
	Total number of turbines	90	...
	Rated voltage (each turbine)	690	V
	Rated frequency	50	Hz
Onshore Grid	Short-circuit Power	2000	MVA
	Base voltage (rms, line-line)	230	kV
	Grid impedance angle	80	degree
Phase reactors	Inductance	0.0239	H
	Resistance	0.0750	Ohm
HVDC System	Line to line DC voltage	200	kV DC
	Power rating	180	MW
HVDC Cable	Cable length	100	km
PMSG wind turbine parameters	Resistance	3e-2	Ohm/km
	Inductance	2e-4	H/km
	Capacitance	2.31e-7	F/km
	C_{dc1}, C_{dc2}	70	μF
	Rated Voltage	690	V
	Rated Frequency	50	Hz
	Stator resistance (Rs)	0.0087	pu
	dq components of the stator inductances (Ld and Lq)	0.135	pu
	Stator flux linkage due to rotor permanent magnet ψ_{pm}	0.95	pu

Biographies

Ali Haghi received the BSc and MSc degrees from University of Kashan, Kashan, Iran, both in Electrical Engineering in 2013 and 2017, respectively. His current research interests include modeling and control of power system dynamics, power electronics and its applications in power systems, and renewable energy systems.

Mohsen Rahimi received his BSc degree in Electrical Engineering in 2001 from Isfahan University of Technology, Isfhan, Iran. He obtained both his MSc and PhD degrees in Electrical Engineering from Sharif University of Technology (SUT), Tehran, Iran in 2003 and 2011, respectively. He joined the Department of Electrical and Computer Engineering at University of Kashan, Kashan, Iran as an Assistant Professor in 2011. Currently, he is an Associate Professor at University of Kashan, and his major research interests include modeling and control of renewable energy sources, wind turbines, and microgrids.